Article

Perfect Nonradiating Modes in Dielectric Nanoparticles

Vasily Klimov

P. N. Lebedev Physical Institute, Russian Academy of Sciences, 53 Leninsky Prospekt, 119991 Moscow, Russia;
klimov256@gmail.com

Abstract: A hypothesis of the existence of perfect nonradiating modes in dielectric nanoparticles of an arbitrary shape is put forward. It is strictly mathematically proved that such modes exist in axisymmetric dielectric nanoparticles and have unlimited radiation Q factors. With the smart tuning of the excitation beams, perfect modes appear as deep minima in the scattered radiation spectra (up to complete disappearance), but at the same time, they have a substantial amplification of the fields inside the particle. Such modes have no analogs and can be useful for the realization of nanosensors, low threshold nanolasers, and other strong nonlinear effects in nanoparticles.

Keywords: high-Q modes; invisibility; perfect nonradiating modes; confined modes; zero scattering; bound states in continuum; Bessel beams

1. Introduction

At present, the properties of dielectric nanoparticles with a high refractive index and low radiative losses are being actively investigated. The physics of optical phenomena in such nanoparticles is very complicated and leads to many interesting applications, such as nanoantennas [1,2], nanolasers [3,4], invisible Mie scatterers [5], sensors [6–9], and nonlinear nanophotonics [10]. As in any other field of physics, all these phenomena are associated with the existence of certain eigenmodes in nanoparticles.

For these applications, modes with strong field localization and low radiation losses are of particular interest. This kind of mode has attracted the most attention of the leading scientific groups.

Firstly, the works devoted to bound states in a continuum (BIC) [11,12] should be mentioned. Due to destructive interference, BIC have no radiation losses at frequencies allowing light propagation in the surrounding space. Theoretical and experimental confirmation of the existence of BIC [11,12] exists only for optical structures that are unlimited in at least one direction, for example, in photonic crystals. A characteristic feature of such modes is the exponential decrease of the fields as the observation point moves away from the surface of the photonic crystal.

The intention to detect undamped modes similar to 2D BIC in 3D particles, that is, in particles limited in all three dimensions, led to a series of studies on the so-called quasi-BIC states [13,14]. The quasi-BIC states have been first discovered in dielectric circular nanocylinders, where they manifest themselves as a significant increase in the radiation Q factor at an optimal ratio between the diameter and the height of the cylinder. The physics of quasi-BIC states do not differ from the physics of usual high-Q quasinormal modes, and their Q factors do not exceed the Q factors of spheres of the same volume. In several works, weakly emitting quasi-BIC states are also called supercavity modes [4,15,16].

Among the works on systems with low radiation losses, there have been investigations of anapole current distributions. The concept of the anapole was introduced by Zel'dovich [17] to designate a current with electromagnetic fields equal to zero where this current is absent. An anapole is the simplest representative of the family of cartesian toroidal (anapole) multipoles, necessary (along with cartesian electric and magnetic multipoles) for a complete description of the field of arbitrary current sources. The cartesian

multipole expansion provides physical insight into the behavior of compact current sources. The relationship between cartesian multipoles and spherical wave function expansions is not one-to-one and is rather complicated [18,19]. An illustrative model of a toroidal anapole can be a torus-shaped solenoid, with the current flowing through its winding. Sometimes such current distributions are called anapole states or even anapole modes. Such definitions, of course, are not correct, since modes, by definition, are solutions of the sourceless Maxwell equations. Nevertheless, there has been research interpreting weakly radiating systems from the point of view of the theory of anapoles [10,13,20–26]. In [27], an exact analytical solution to the problem of the scattering of a Bessel beam by a spherical particle was found, and using this solution it was shown that the scattering intensity can be reduced to arbitrarily small values.

Despite the active search for non-trivial nonradiating modes in 3D dielectric particles, the exact solutions of sourceless Maxwell equations justifying the existence of such modes have not been known. In this work, we fill this gap, and strictly mathematically show that there are unparalleled perfect nonradiating modes in dielectric nanoparticles, as well as propose a regular method for finding such modes in arbitrary dielectric particles.

2. Materials and Methods

Usually, the quasinormal modes are found by solving sourceless Maxwell equations

$$
\begin{aligned}
\nabla \times \mathbf{E}_1 &= ik_0\mathbf{H}_1; \nabla \times \mathbf{H}_1 = -ik_0\varepsilon\mathbf{E}_1, \text{inside nanoparticle} \\
\nabla \times \mathbf{E}_2 &= ik_0\mathbf{H}_2; \nabla \times \mathbf{H}_2 = -ik_0\mathbf{E}_2, \text{outside nanoparticle} \\
\mathbf{n} \times (\mathbf{E}_1 - \mathbf{E}_2) &= 0; \mathbf{n} \times (\mathbf{H}_1 - \mathbf{H}_2) = 0, \text{at the boundary}
\end{aligned}
\tag{1}
$$

with the Sommerfeld radiation conditions at infinity [28]:

$$
\mathbf{E}_2(\mathbf{r}, k_0) \rightarrow \frac{\exp(ik_0r)}{r}\mathbf{F}(\mathbf{k})
\tag{2}
$$

where ε is the nanoparticle permittivity, $\mathbf{r}$ is the position vector, $r = |\mathbf{r}|$, $\mathbf{F}(\mathbf{k})$ is the scattering amplitude, $k_0 = \omega/c$ is the wavenumber in a vacuum, ω is the frequency, c is the speed of light, and $\mathbf{k}$ is the unit vector in the direction of observation.

Within this approach, any field component $E(r, \theta, \varphi, k_0)$ outside the resonator should be expanded over spherical harmonics $Y_n^m(\theta, \varphi)$ and spherical Hankel functions $h_n^{(1)}(k_0r)$:

$$
E(r, \theta, \varphi, k_0) = \sum_{n,m} a_{nm}h_n^{(1)}(k_0r)Y_n^m(\theta, \varphi)
\tag{3}
$$

where a_{nm} are expansion coefficients which can be obtained from the boundary conditions.

Spherical Hankel functions $h_n^{(1)}(k_0r)$ are singular at $r = 0$ (inside the resonator) and fundamentally related to radiation and radiative losses. Moreover, such modes grow unlimitedly at infinity, requiring the development of very complex artificial approaches for their use.

However, finding all the modes is a non-trivial task, not only from a computational point of view, and the quasinormal modes in optics and the eigenstates in quantum mechanics do not exhaust the entire set of modes that exist in a system. For example, in quantum mechanics, a strange stationary solution of the Schrödinger equation with an eigenvalue above the barrier ($E > 0$) was demonstrated in the seminal paper [29] (see also [30]). In the limit $r \rightarrow \infty$, this "strange mode" does not decrease exponentially and can be presented as a superposition of nonsingular spherical Bessel functions j_n:

$$
\psi(r) = \sum_n a_n j_n(r) = -\frac{1}{105}(3j_4(r) + 10j_2(r) + 7j_0(r)) + \ldots
\tag{4}
$$

The problem of finding the eigenfrequencies in optics is like solving the Schrödinger equation with the potential $V = k_0^2(1 - \varepsilon(\mathbf{r})), \varepsilon(\mathbf{r}) > 1$ and the eigenvalue $E = k_0^2 > 0$

above the barrier. This analogy allows us to generalize the approach of Neumann–Wigner [29] to the case of electromagnetic fields and present a new class of electromagnetic eigenmodes— perfect nonradiating modes. To find them, we propose to use the solutions of Maxwell's equations, not containing waves that carry energy away in principle! More specifically, we suggest looking for the electromagnetic fields outside the particle in the form of a super-position of solutions of Maxwell's equations that are nonsingular in unlimited free space, including the interior of the nanoparticle. This approach is fundamentally different from the usual one, assuming that the functions describing the fields outside the body can have singularities upon analytic continuation into its interior (see (3)). We propose, however, to use only the field components nonsingular at the origin to describe the fields outside the nanoparticle to find the perfect nonradiating modes. For example, one can look for fields outside the resonator in the form of spherical harmonics expansion

$$E(r, \theta, \varphi, k_0) \;=\; \sum a_{nm} j_n(k_0 r) Y_n^m(\theta, \varphi) \tag{5}$$

where $j_n(k_0 r)$ are nonsingular spherical Bessel functions or in the form of plane waves expansion

$$E(\mathbf{r}, k_0) \;=\; \int d^3 \mathbf{k}\, a(\mathbf{k}) \delta\left(k^2 - k_0^2\right) e^{i\mathbf{rk}} \tag{6}$$

Obviously, if a solution of Maxwell's equations with outside fields in the form (5) or (6) exists, then, in principle, it does not have a flux of energy and radiation. Since (5) or (6) have no singularities in the entire space (including the nanoparticle interior), the finding of modes in infinite space can be reduced to the internal problem of finding fields in the volume of a nanoparticle only. As a result, the system of equations that determine unambiguously the perfect nonradiating modes in a nonmagnetic nanoparticle with the permittivity ε can be written as a system of two equations for two independent auxiliary fields $\mathbf{E}_1$ and $\mathbf{E}_2$:

$$
\begin{aligned}
\nabla \times \mathbf{E}_1 \;&=\; ik_0 \mathbf{H}_1;\; \nabla \times \mathbf{H}_1 \;=\; -ik_0\varepsilon \mathbf{E}_1,\, \text{inside nanoparticle} \\
\nabla \times \mathbf{E}_2 \;&=\; ik_0 \mathbf{H}_2;\; \nabla \times \mathbf{H}_2 \;=\; -ik_0 \mathbf{E}_2,\, \text{inside nanoparticle} \\
\mathbf{n} \times (\mathbf{E}_1 - \mathbf{E}_2) \;&=\; 0;\; \mathbf{n} \times (\mathbf{H}_1 - \mathbf{H}_2) \;=\; 0,\, \text{at the boundary}
\end{aligned}
\tag{7}
$$

It is important to note that system (7) is a closed interior problem of mathematical physics, and there is no need to impose any boundary condition at infinity to solve it!

At some real values of frequency k_0, the system of Equation (7) becomes compatible, that is, the perfect nonradiating modes appear. It is very important that, due to a specific structure of (7), there is nothing common between the frequencies of perfect modes and the frequencies of usual quasinormal modes. The modes found from (7) are orthogonal in the sense that

$$\int\limits_V dV(\varepsilon \mathbf{E}_{1,n} \cdot \mathbf{E}_{1,m} - \mathbf{E}_{2,n} \cdot \mathbf{E}_{2,m}) \;=\; \delta_{nm} \tag{8}$$

where the integration is over the nanoparticle volume V. The condition (8) is also drastically different from orthogonality conditions for usual normal modes.

The physical (observable) fields inside the nanoparticle are determined by $\mathbf{E}_1, \mathbf{H}_1$, while the physical fields outside the particle are determined by the analytic continuation of the $\mathbf{E}_2, \mathbf{H}_2$ from the interior domain.

The system of Equation (7) is not elliptic at any k_0, and in a general case, a rigorous mathematical theory does not yet exist for it. Nevertheless, we managed to find conditions for the existence of perfect nonradiating modes for arbitrary spheres, spheroids, and superspheroids, describing well practically all forms of nanoparticles that are interesting for applications.

The perfect nonradiating modes are not abstract solutions of sourceless Maxwell equations. They are of great practical importance for finding the conditions for extremely small or even zero scattered power at finite stored energy, leading to the unlimited Q factor.

Indeed, if the fields $\mathbf{E}_1$ and $\mathbf{E}_2$ are solutions of (7), then it can be shown that when the incident field is exactly equal to field $\mathbf{E}_2$, the scattered field will be zero, but the field $\mathbf{E}_1$ inside the particle will be different from zero, that is, the perfect nonradiating mode with the unlimited Q factor will be excited. Therefore, perfect nonradiating modes can also be referred to as "perfect non-scattering modes". Of course, it is difficult to realize the nonsingular field $\mathbf{E}_2$ in an experiment exactly, and therefore the best possible approximation should be used. With a good approximation, the quality factor will be very large.

We emphasize once again that in the present work, solutions of the Maxwell equations are considered, where the fields (5) and (6) outside the nanoresonator are nonsingular with analytical continuations inside. However, along with perfect modes (5), (6), and (7) there is a nonradiating mode continuum, the external fields of which can be represented as an expansion in terms of spherical Bessel and Neumann functions y_n:

$$E(r, \theta, \varphi, \omega) = \sum [a_{nm} j_n(k_0 r) + b_{nm} y_n(k_0 r)] Y_n^m(\theta, \varphi) \tag{9}$$

where a_{nm}, b_{nm} are some expansion coefficients which can be obtained from the boundary conditions.

The external fields (9) have a singularity when they are analytically continued inside the nanoparticle, and therefore the modes corresponding to them do not possess the main property of the perfect nonradiating modes found by us—the absence of scattering or invisibility, since scattering is large at their eigenfrequencies. Therefore, such solutions are not considered in this article.

Our results are very general and are applicable within arbitrary frequency ranges, where the permittivity can vary over a wide range. For example, Si has a permittivity of $\varepsilon = 12$–16 in the visible and infrared ranges [31], PbTe has a permittivity of $\varepsilon = 36$ in the infrared range [32], and Bi_2Te_3 has exceptionally high permittivity ranging between 50 and 60 throughout the 2–10 μm region [33]. With this in mind, we built graphs for a variety of permittivities.

3. Result

3.1. TM Perfect Nonradiating Modes in Spherical Particles

3.1.1. Analytical Solutions

First of all, perfect nonradiating modes exist for a spherical particle of the radius R, having the following solution of the system (7) for TM polarization (for details see Appendix A):

$$\begin{aligned} H_\varphi &= j_n(z_0) j_n\left(k_0 \sqrt{\varepsilon} r\right) P_n^1(\cos \theta), r < R \\ H_\varphi &= j_n(z_1) j_n(k_0 r) P_n^1(\cos \theta), r > R \\ z_0 &= k_0 R; z_1 = k_0 \sqrt{\varepsilon} R \end{aligned} \tag{10}$$

The condition for the existence of perfect nonradiating modes (10) has the form

$$\varepsilon j_n(z_1)[z_0 j_n(z_0)]' = j_n(z_0)[z_1 j_n(z_1)]' \tag{11}$$

and coincides with the vanishing of the numerator of the Mie scattering coefficient.

The dispersion Equation (11), along with complex roots, also has real roots, corresponding to perfect nonradiating modes. Figure 1 shows the dependences of $\text{Re}\left(H_\varphi(r, \theta = \pi/2)\right)$ on the radius for a perfect nonradiating mode and a usual quasinormal mode with radiation losses.

Figure 1 shows that the quasinormal mode grows exponentially at infinity, while the perfect nonradiating mode goes to zero and has no radiation losses! Inside the resonator, the spatial structures of these modes are similar. It can be seen also from this figure that the spatial structure of the perfect mode does not change practically even in the case of large internal losses (Joule and other). Table 1 shows Q factors of the PTM_{101} and TM_{101} modes for a silicon sphere at various wavelengths.
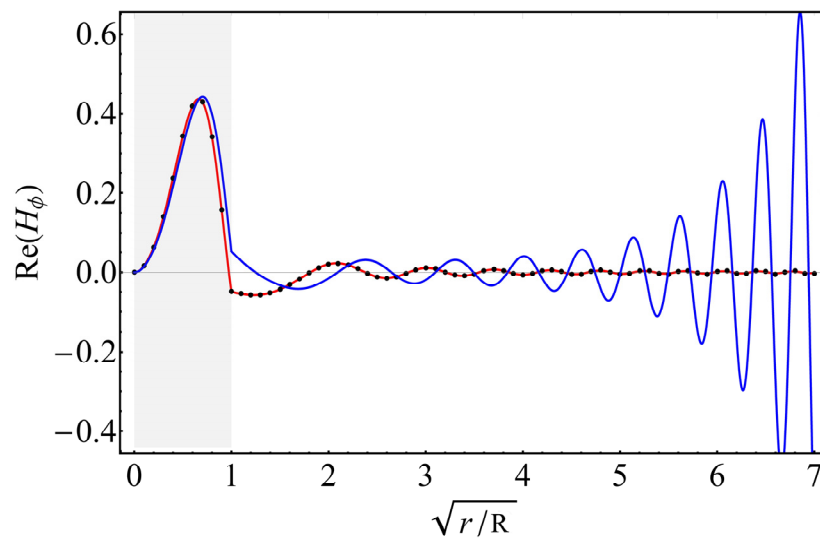
Figure 1. The dependence of $\mathrm{Re}\left(H_\varphi(r, \theta = \pi/2)\right)$ on the radius for the usual TM_{101} mode (blue, $k_0 R = 1.22332 - 0.12557\,i$, $\varepsilon = 12$), for the perfect nonradiating PTM_{101} mode ((10), red, $k_0 R = 1.36687$, $\varepsilon = 12$) and for the perfect nonradiating PTM_{101} mode in a sphere with large losses ((10), black dots, $k_0 R = 1.36568 - 0.0323\,i$, $\varepsilon = 12 + 0.5\,i$).

Table 1. Q factors of the PTM_{101} and TM_{101} modes in the Si sphere.

Wavelength, nm	Si Permittivity	$Q_{\mathbf{PTM101}}$	$Q_{\mathbf{TM101}}$
500	$18.3932 + 0.416393\,i$	42	32
600	$15.4524 + 0.145612\,i$	101	36
800	$13.4615 + 0.0386382\,i$	327	32
1000	$12.7806 + 0.00350493\,i$	3402	30
1200	$12.4045 + 9.79398 \times 10^{-7}\,i$	1.2×10^7	27

It follows from Table 1 that the Q factors of the perfect modes, even in the case of substantial Joule losses, significantly exceed the Q factors of usual quasinormal modes.

Figure 2 shows the spatial distribution of the excitation field

$$H_\varphi = j_n(z_1) j_n(k_0 r) P_n^1(\cos\theta), \quad 0 < r < \infty \tag{12}$$

without any nanoresonator and the full field in the presence of nanoresonator at the frequency of the perfect nonradiating PTM_{11} mode (see (11)).

Figure 2 shows clearly that the mounting of a nanoparticle into the excitation field (12) does not affect the field outside it; that is, at this frequency, the nanoparticles are invisible.
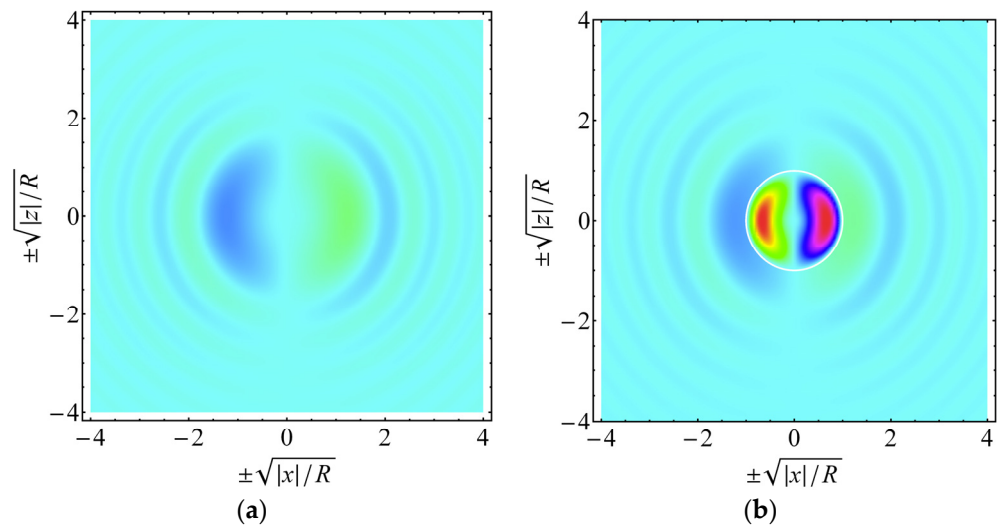
Figure 2. (**a**) Spatial distribution of the excitation field (12) at the frequency of the perfect nonradiating mode PTM$_{11}$ and (**b**) full field (10) in the presence of nanoparticle ($n = 1$, k_0R = 1.36687, $\varepsilon = 12$).

3.1.2. Manifestation of Perfect Nonradiating Modes in Scattering Experiments

The realization of a spherical standing wave (12) in an experiment is a difficult task, and, therefore, to observe TM perfect nonradiating modes in the sphere, we have performed the Comsol simulations with an incident Bessel beam:

$$
\begin{aligned}
H_\varphi &= J_1(k_0\rho\sin\alpha)e^{ik_0 z\cos\alpha}, \text{ running wave} \\
H_\varphi &= J_1(k_0\rho\sin\alpha)\cos(k_0 z\cos\alpha), \text{ standing wave}
\end{aligned}
\tag{13}
$$

In (13), ρ and z are cylindrical coordinates and α is a conical angle of the Bessel beam. In the vicinity of the origin of coordinates, such a beam approximates the perfect nonradiating mode (12) well. To solve the Maxwell equations within the Comsol Multiphysics software, we used the Radio Frequency interface → Electromagnetic Waves, Frequency Domain → the scattered field formulation. Field (13) was used as a background field. The geometry of the scattering problem and corresponding mesh are shown in Figures 3 and 4.

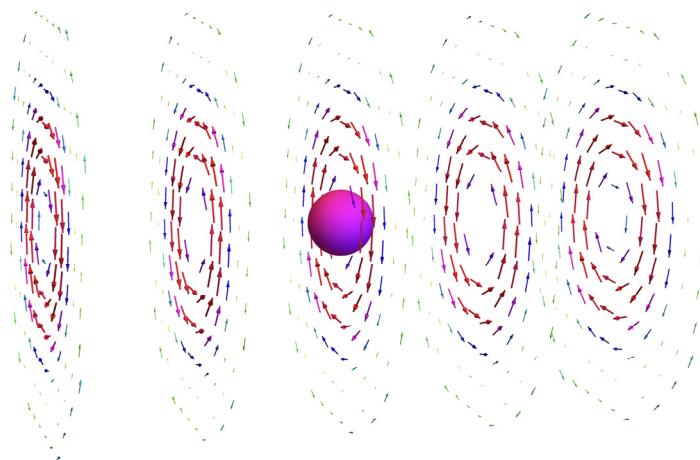The results of the simulations are shown in Figure 5.

Figure 3. A nanoparticle inside an incident Bessel beam (13). Arrows show ReH_φ distribution.
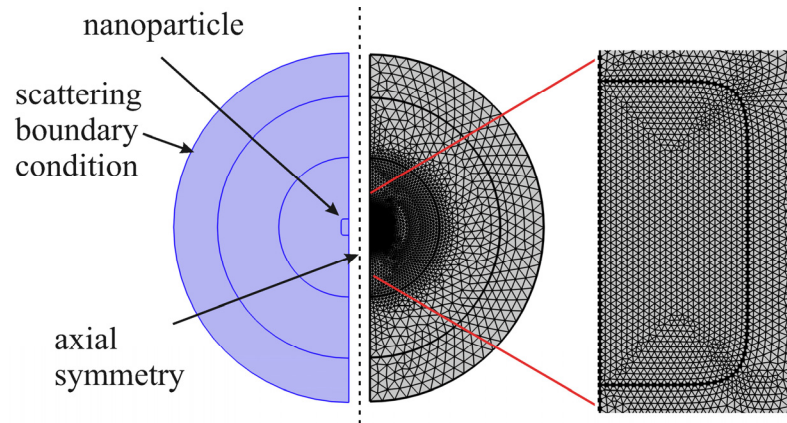
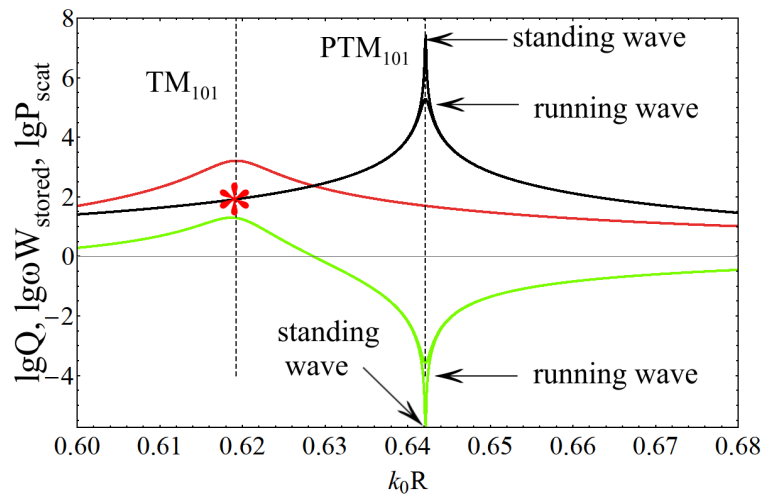**Figure 4.** Geometry and a mesh of the Comsol simulation.

Figure 5. The dependence of scattered power P_{scat} (green), stored energy W_{stored} (red), and generalized radiation quality factor $Q = \omega W_{stored}/P_{scat}$ (black) on the size parameter of a sphere obtained within the Comsol simulation. TM excitation (13), $\alpha = \text{atan}(2)$, $\varepsilon = 50$ (Bi_2Te_3). The asterisk on the red curve shows the Q factor value of the TM_{101} mode.

Figure 5 shows clearly the appearance of an extremely high-quality perfect PTM_{101} mode in the spectra of a Bessel beam (13) scattered by a sphere. Note that the Q factor of the PTM_{101} mode is three orders (five orders for standing wave) of magnitude greater than the Q factor of a usual TM_{101} mode! This figure also shows a significant influence of the spatial structure of the excitation beam on the Q factors of the perfect nonradiating modes.

3.2. TM Perfect Nonradiating Modes in Spheroidall Particles

3.2.1. Analytical Solutions

Nonradiating modes are not a feature of spherical geometry and exist for axisymmetric open dielectric resonators of an arbitrary shape. We have shown rigorously that such modes exist for arbitrary spheroids with semiaxes a and b, having a volume equal to the volume of a sphere of the radius R with a surface described by the equation

$$(\rho/b)^2 + (z/a)^2 = 1; ab^2 = R^3 = const \qquad (14)$$

The eigenfunctions and eigenvalues of perfect nonradiating modes of such spheroids can be found by expanding the solutions of the Equation (7) over spheroidal functions [34,35]. In the case of TM polarization for a prolate spheroid, $a/b > 1$, the general axisymmetric solu-

tion of Maxwell's equations [34,35] in the prolate coordinate system ($1 < \xi < \infty$, $-1 < \eta < 1$, $0 < \varphi < 2\pi$) has the form:

$$
\begin{aligned}
H_{1,\varphi} &= \sum_{n=1}^{\infty} a_n PS_{n1}(c_1,\eta) S_{n1}(c_1,\xi), 1 < \xi < \xi_0 \text{(inside NP)} \\
H_{2,\varphi} &= \sum_{n=1}^{\infty} b_n PS_{n1}(c_0,\eta) S_{n1}(c_0,\xi), 1 < \xi < \infty \text{(everywhere)}
\end{aligned}
\tag{15}
$$

where $PS_{n1}(c,\eta)$ are the angular spheroidal functions and $S_{n1}(c,\xi)$ are the radial spheroidal functions of the first kind, $\xi_0 = a/\sqrt{a^2 - b^2}$ and $c_{0,1} = z_{0,1}(b/a)^{1/3}/\xi_0$. For details see Appendix B.

Equating the tangential components of the electric and magnetic fields on the surface of the spheroid (14) and using the orthogonality of angular spheroidal functions, one can find the dispersion equation describing the perfect nonradiating modes:

$$
\begin{aligned}
\det M &= 0, \quad M_{np} = \Pi_{np}(c_1,c_0) \times \\
&\left(\varepsilon SD_p(c_0,\xi_0) S_{n1}(c_1,\xi_0) - S_{p1}(c_0,\xi_0) SD_n(c_1,\xi_0) \right)
\end{aligned}
\tag{16}
$$

$$
\begin{aligned}
\Pi_{n,p}(c_1,c_0) &= \int_{-1}^{1} d\eta \, PS_{n1}(c_1,\eta) \times PS_{p1}(c_0,\eta) \\
SD_n(c,\xi_0) &= \partial_{\xi_0}\left(\sqrt{\xi_0^2 - 1} \times S_{p1}(c,\xi_0) \right)
\end{aligned}
\tag{17}
$$

The dispersion Equation (16) is also valid for an oblate spheroid with the corresponding analytic continuation of spheroidal functions.

The exact solution of the dispersion Equation (16) for perfect TM modes (PTM) is shown in Figure 6. This figure also shows the dispersion laws of usual TM modes and so-called confined modes [36] with a magnetic field different from zero only inside the nanoparticle and complying with the equations:

$$
\begin{aligned}
\nabla \times \nabla \times \mathbf{H}_n &= \varepsilon k_{0n}^2 \mathbf{H}_n, \text{ inside nanoparticle} \\
\mathbf{H}_n &= 0, \text{ at the boundary}
\end{aligned}
\tag{18}
$$

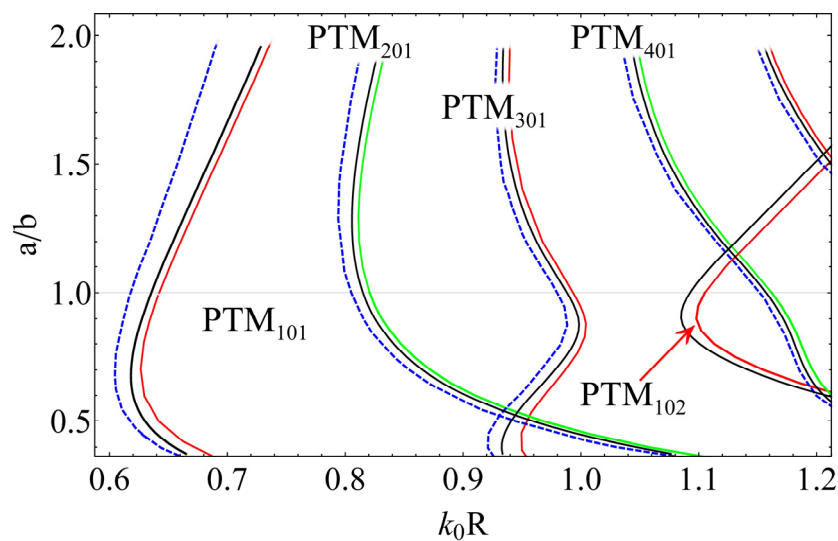and the electric field of the confined modes is zero everywhere.

Figure 6. Perfect nonradiating TM modes (PTM) of spheroids with $\varepsilon = 50$ (Bi_2Te_3) as a function of the size parameter k_0R and the spheroid aspect ratio, a/b. Red and green curves stand for odd and even perfect nonradiating modes, blue dashed lines correspond to usual quasinormal modes. Black curves show the frequencies of confined modes (18), $\omega_{n,confined} = k_{0n}c$.

It can be seen from Figure 6, that for each usual quasinormal mode (blue dashed curves), there are its counterparts in the form of a perfect nonradiating mode (red and green curves), indicating that there are infinitely many perfect nonradiating modes. It should be emphasized here once again that the eigenfrequencies of the perfect nonradiating modes, the solution of (16), are real numbers!

Another interesting fact is that the eigenfrequencies of perfect nonradiating modes are substantially higher than the real parts of frequencies of usual modes $\omega_{n,usual}$. Moreover, it can be argued that the frequencies of confined modes (18), $\omega_{n,confined} = k_{0n}c$ (black curves), appearing in the limit $\varepsilon \to \infty$, are always situated between the frequencies of usual and perfect nonradiating modes, $\omega_{n,usual} < \omega_{n,confined} < \omega_{n,perfect}$. This relationship between frequencies is a manifestation of a very deep connection between confined modes (with fields localized strictly inside the resonator) and perfect nonradiating modes (with fields not localized inside the resonator).

Figure 7 shows the dependence of the frequencies $k_0 R \sqrt{\varepsilon}$ of usual and perfect nonradiating modes on the inverse permittivity.
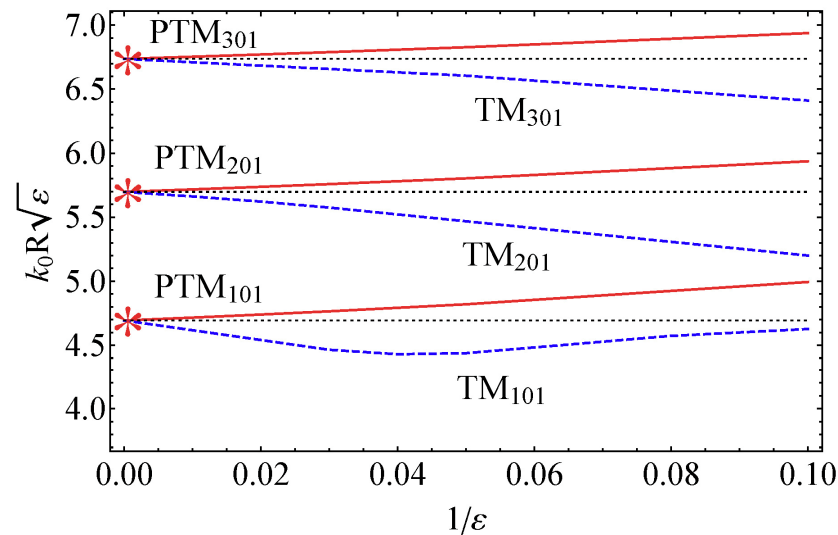

Figure 7. Dependence of $k_0 R \sqrt{\varepsilon}$ for usual (blue dashed curves, TM) and perfect nonradiating modes (red curves, PTM) on $1/\varepsilon$ for a prolate spheroid with $a/b = 1.3$. The red asterisks and black dashed lines indicate confined modes (18).

From Figure 7, it is seen that in the limit $\varepsilon \to \infty$, the usual and perfect nonradiating modes merge into confined ones. However, at finite permittivities, this degeneracy is lifted, and confined modes are split into perfect nonradiating modes with infinite Q factors and the usual quasinormal modes with finite Q factors. From Figures 6 and 7 one can clearly see that there is nothing common between the frequencies of perfect nonradiating modes and the frequencies of quasinormal modes.

Such an unambiguous connection between the frequencies of confined modes and perfect nonradiating modes allows us to assert that perfect nonradiating modes with TM polarization definitely exist for any axisymmetric dielectric bodies!

After the eigenvalues are found, the eigenfunctions of the perfect nonradiating modes can be found.

For example, the solution of (15) and (16) for PTM$_{101}$ mode in a prolate spheroid with $\varepsilon = 10$ and $a/b = 1.3$ is as follows: $k_0 R = 1.57757$, $a_1 = -7.22705$, $a_3 = 0.0924$, $a_5 = 0.004323$, $a_7 = 0.00019$, $b_1 = 1$, $b_3 = -0.59122$, $b_5 = 1.08884$, and $b_7 = -2.81192$ and is shown in Figure 8.

A comparison of Figures 1, 2b and 8 shows that the structure of a perfect nonradiating mode in a spheroid looks generally similar to the structure of a perfect nonradiating mode in a sphere.
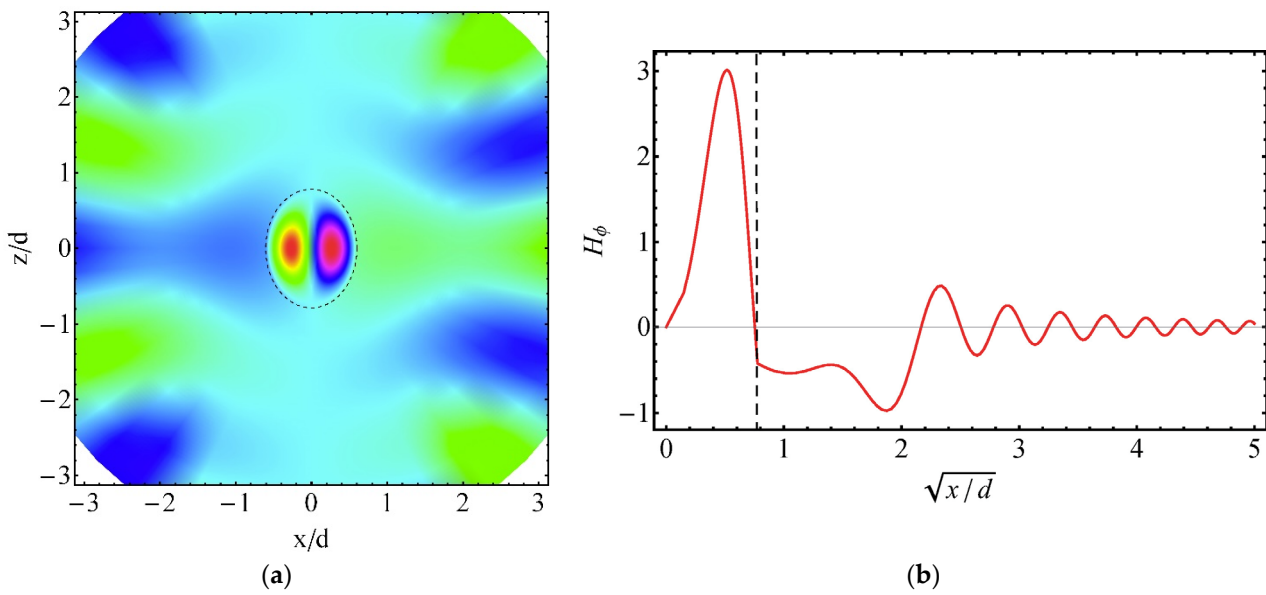
(a)   **(b)**

Figure 8. (**a**) Spatial distribution of H_{φ} (*x*,*z*) and (**b**) the dependence of H_{φ} (*x*,*z* = 0) on *x* (**right**) in the PTM_{101} mode in a prolate spheroid with $\varepsilon = 10$, $k_0 R = 1.57757$, $k_0 d = 2.4$, $a/b = 1.3$.

3.2.2. Manifestation of TM Perfect Nonradiating Modes in Scattering Experiments

To demonstrate the great practical importance of the perfect nonradiating modes in spheroids, we have simulated within Comsol Multiphysics software the scattering of an axially symmetric Bessel beam by nanospheroids of different shapes. To observe the even perfect nonradiating modes, we have used an even incident Bessel beam:

$$H_{\varphi} \sim J_1(k_0 \sin \alpha \rho) \cos(k_0 z \cos \alpha) \tag{19}$$

In (19), ρ and z are cylindrical coordinates and α is a conical angle of the Bessel beam. In the vicinity of the origin of coordinates, such a beam approximates the perfect nonradiating mode (15) well.

Let us stress that the Comsol simulations are fully independent of our analytical results (16) and (17) and fully confirm them.

In Figure 9 one can see the simulated dependence of scattered power P_{scat}, stored energy W_{stored}, and the generalized radiation quality factor $Q = \omega W_{stored}/P_{scat}$, on the size parameter of nanospheroids for aspect ratio $a/b = 0.7$.

Figure 9 clearly shows the presence of perfect nonradiating modes, having Q factors significantly higher than the Q factors of usual quasinormal modes. It can be seen from this figure that, upon excitation (19), all the maxima of the generalized Q factor are due to the perfect nonradiating modes shown in Figures 6 and 7. In this case, the Q factors of usual modes (shown by asterisks) are several orders of magnitude lower than the Q factors of perfect nonradiating modes! Moreover, smart optimization of the excitation beam [27] makes it possible to increase the Q factor of perfect nonradiating modes almost unlimitedly.
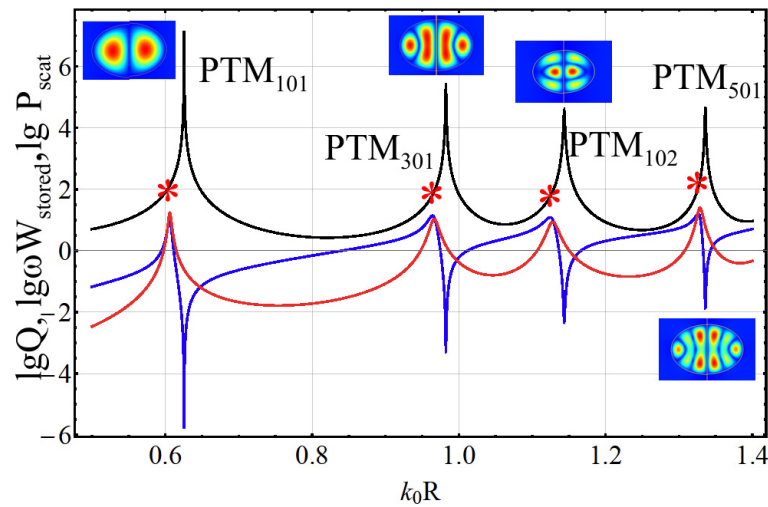
Figure 9. The dependence of logarithms of scattered power P_{scat} (blue), stored energy W_{stored} (red), and radiation quality factor $Q = \omega W_{stored}/P_{scat}$ (black) on the size parameter of an oblate spheroid with $a/b = 0.7$ obtained within the Comsol simulation. TM symmetric excitation (19), $\alpha = \pi/4$, $\varepsilon = 50$ (Bi_2Te_3). The insets show the distribution of $|H\varphi|$ in perfect nonradiating modes. All maxima correspond to perfect nonradiating modes! The red asterisks on the black curve show the Q factor of the usual quasinormal modes.

3.3. TE Perfect Nonradiating Modes in Spheroidall Particles

3.3.1. Analytical Solutions

In this case, the only nonzero component of the electric field can be written in the form:

$$
\begin{aligned}
E_{1,\varphi} &= \sum_{n=1}^{\infty} a_n PS_{n1}(c_1,\eta)S_{n1}(c_1,\xi), c_1 = k_0R\sqrt{\varepsilon}\sqrt{t^2-1}/t^{1/3} \text{ inside nanoparticle}, 1 < \xi < \xi_0 \\
E_{2,\varphi} &= \sum_{n=1}^{\infty} b_n PS_{n1}(c_0,\eta)S_{n1}(c_0,\xi), c_0 = k_0R\sqrt{t^2-1}/t^{1/3} \text{ everywhere}, \xi > 1
\end{aligned}
\tag{20}
$$

Equating the tangential components of the electric and magnetic fields on the surface of the spheroid (14) and using the orthogonality of angular spheroidal functions, one can find the dispersion equation describing the TE perfect nonradiating modes:

$$
\begin{aligned}
\det M^{TE} &= 0, \ M_{np}^{TE} = \Pi_{np}(c_1,c_0) \times \\
&\left(SD_p(c_0,\xi_0)S_{n1}(c_1,\xi_0) - S_{p1}(c_0,\xi_0)SD_n(c_1,\xi_0)\right)
\end{aligned}
\tag{21}
$$

which differs from the dispersion Equation (16) only by the absence of ε in the parenthesis.

The exact solution of the dispersion Equation (21) for perfect TE modes (PTE) is shown in Figure 10.

From Figure 10 and the structure of the dispersion Equation (21), it follows that the number of perfect nonradiating modes with TE polarization is infinite, as in the case of TM polarization.

It is clearly seen from Figure 10, that the frequencies of the perfect nonradiating modes with TE polarization are located very far from the frequencies of the usual TE modes of similar symmetry, indicating that there is no connection between usual and perfect modes.

3.3.2. Manifestation of TE Perfect Nonradiating Modes in Scattering Experiments

Demonstration of the existence of TE perfect nonradiating modes in scattering spectra is more complicated in comparison with the TM case since perfect modes with TE polarization are not confined modes [36] in the limit $\varepsilon \to \infty$. In addition, the frequencies of perfect $PTE_{n,0,1}$ modes turn out to be close to the frequencies of usual $TE_{n+2,0,1}$ modes. Therefore, to demonstrate perfect nonradiating TE modes, an incident beam should not excite the usual nearby modes. In particular, to demonstrate the existence of the PTE_{101} mode (see

Figure 11), it is necessary to suppress the excitation of the usual TE_{301} mode by using an exciting field of the form:

$$E_\varphi(r,\theta) \sim \left(j_1(k_0 r) P_1^1(\cos\theta) + \xi\, j_3(k_0 r) P_3^1(\cos\theta) \right) \qquad (22)$$

In (22), r and θ are spherical coordinates and $j_n(x)$ and $P_n^1(z)$ are the spherical Bessel functions and the Legendre polynomial, correspondingly.
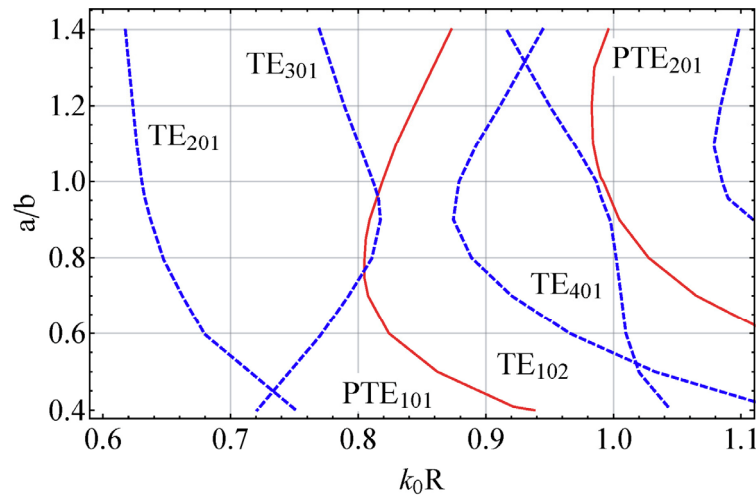

Figure 10. Perfect nonradiating TE modes of spheroids with $\varepsilon = 50$ as a function of the size parameter $k_0 R$ and the aspect ratio, a/b. Red curves stand for TE perfect nonradiating modes (PTE) and blue dashed lines correspond to usual quasinormal TE modes.
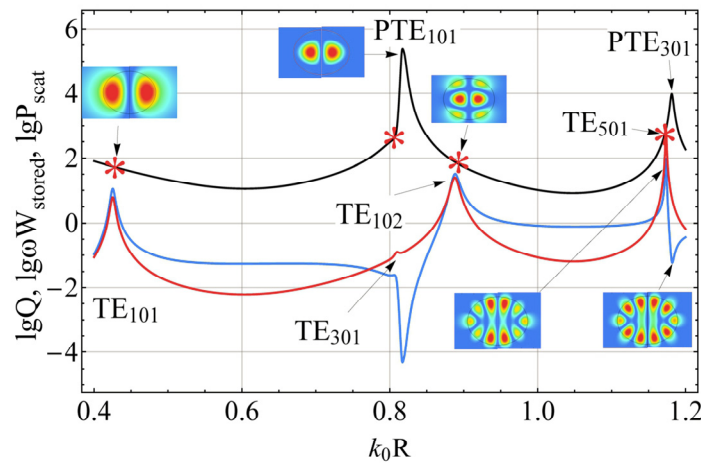

Figure 11. The dependence of logarithms of scattered power (blue), stored energy (red), and generalized quality factor $Q = \omega W_{stored}/P_{scat}$ (black) on the size parameter of nanoparticles simulated within Comsol Multiphysics. TE excitation (22), $\xi = -9.915$, $\varepsilon = 50$, $a/b = 0.8$ (oblate spheroid). The insets show the distribution of $|E_\varphi|$ corresponding to the maxima of stored energy or Q-factor. The asterisks on the black curve show the Q factor values of the usual modes.

Figure 11 clearly shows the presence of the perfect nonradiating modes, having Q factors significantly higher than the Q factors of usual modes. Moreover, smart optimization of the excitation beam [27] makes it possible to increase the Q factor of the perfect nonradiating modes unlimitedly (with the neglect of Joule losses in the nanoparticle material, of course).

3.4. TM Perfect Nonradiating Modes in Cylindrical Particles

We have not yet succeeded in finding an analytical solution for perfect nonradiating modes in a dielectric cylinder of a finite height. However, proceeding from the very plausible hypothesis that the existence of perfect modes is associated with the existence of confined modes, we have found the frequencies of perfect nonradiating modes by the Comsol simulation of the scattering of a Bessel beam

$$H_\varphi \sim J_1(k_0 \sin \alpha \rho) \cos(k_0 z \cos \alpha) \qquad (23)$$

by a superspheroid with the surface described by the equation:

$$(\rho/a(t))^t + (z/c(t))^t = 1 \qquad (24)$$

For $t = 2$, this is a sphere. For $t = \infty$, this is a cylinder with the diameter $D_{cyl} = 2a\,(\infty)$ and the height $H_{cyl} = 2c\,(\infty)$.

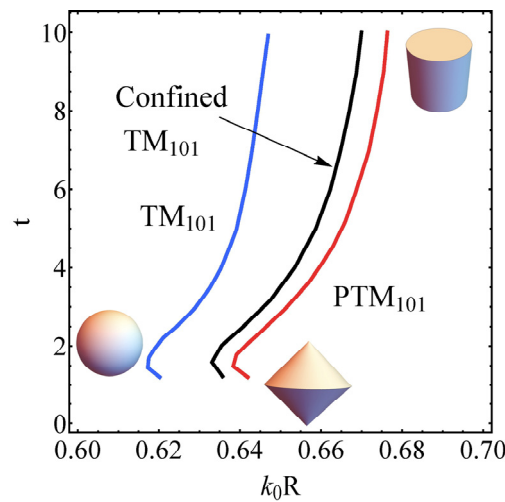The results of the Comsol simulation are shown in Figure 12.

Figure 12. Perfect nonradiating PTM modes of superspheroids with $\varepsilon = 50$ as a function of the size parameter, $k_0 R$, and the shape parameter, t. The red curve stands for PTM$_{101}$ perfect nonradiating mode (PTM) and the blue line corresponds to the usual TM$_{101}$ mode. The black curve corresponds to the confined ($\varepsilon \to \infty$) TM$_{101}$ mode (18).

It is clearly seen from Figure 12 that the frequencies of the perfect nonradiating modes with TM polarization in superspheroids are located very far from the frequencies of the usual modes of similar symmetry, indicating that there is no connection between the usual and perfect modes.

In Figure 13, one can see the dependence of scattered power, stored energy, and generalized Q factor on the size parameter $k_0 R$ of a superspheroid with shape parameter $t = 8$, when excited by a Bessel beam (23).

Figure 13 shows that all the maxima of the generalized Q factor with the excitation (23) are due to perfect nonradiating modes, with Q factors of several orders of magnitude higher than the Q factors of usual modes.

Note that in Figures 12 and 13, the scattering minimum is shifted to the high-frequency region relative to the stored energy maximum. A similar shift was found in the experimental work [26], where silicon disks were illuminated on-chip at telecom wavelengths.
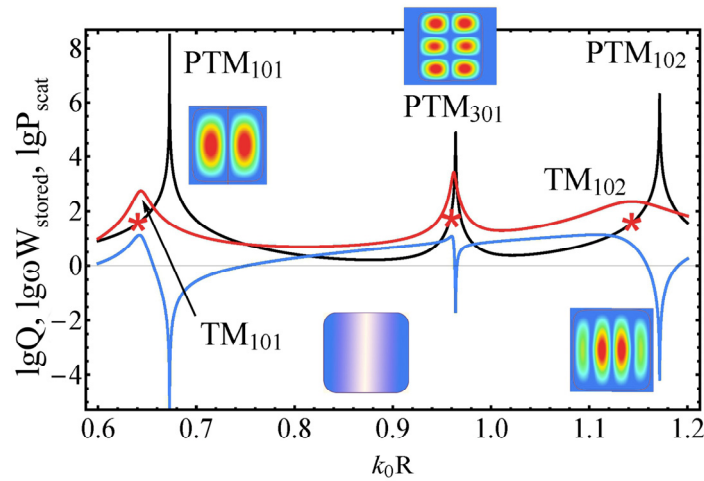
Figure 13. The dependence of logarithms of scattered power (blue), stored energy (red), and radiation quality factor $Q = \omega W_{stored}/P_{scat}$ (black) on the size parameter of a superspheroid with $D/H = 0.96$, $t = 8$ obtained as a result of the Comsol simulation. TM symmetric excitation (23), $\varepsilon = 50$, $\alpha = \pi/4$. The insets show the field distribution of the perfect nonradiating modes and the cross-section of the investigated superspheroid. All maxima correspond to perfect nonradiating modes! The stars on the black curve show the Q factor values of the usual modes.

4. Discussion

Above, as an example, perfect nonradiating PTM and PTE modes in dielectric spheroidal nanoparticles are considered. However, this approach can be directly generalized to waveguides [37]. Moreover, this approach can be directly generalized to nanoparticles made from double negative (DNG) or chiral metamaterials.

The system of equations for finding perfect nonradiating modes without boundary conditions at infinity (a generalization of the system (7)) in this case has the form:

$$\nabla \times \mathbf{E}_1 = ik_0\mu(\mathbf{H}_1 + \eta\nabla \times \mathbf{H}_1); \nabla \times \mathbf{H}_1 = -i\varepsilon k_0(\mathbf{E}_1 + \eta\nabla \times \mathbf{E}_1), \text{inside nanoparticle}$$
$$\nabla \times \mathbf{E}_2 = ik_0\mathbf{H}_2; \nabla \times \mathbf{H}_2 = -ik_0\mathbf{E}_2, \text{everywhere} \tag{25}$$
$$\mathbf{n} \times (\mathbf{E}_1 - \mathbf{E}_2) = 0; \mathbf{n} \times (\mathbf{H}_1 - \mathbf{H}_2) = 0, \text{at the boundary}$$

where $\mathbf{E}$ and $\mathbf{H}$ are the inductions and the strengths of electric and magnetic fields, correspondingly, ε and μ are the permittivity and the permeability of the chiral medium, and η is the dimensional parameter of chirality. The solution of the system (25) in the case of a chiral spherical resonator can be found using the method described in [38].

However, the existence of perfect nonradiating modes for non-symmetric nanoparticles is still questionable.

Thus, we have put forward the hypothesis of the existence of perfect nonradiating eigenmodes of light in dielectric nanoparticles. These modes are the exact solutions of sourceless Maxwell equations. We have shown rigorously that in the case of axisymmetric particles, such modes always exist and arise at frequencies somewhat higher than the resonance frequencies of usual quasinormal modes.

In a spherical case, the problem of finding perfect nonradiating modes can be reduced to the scattering problem, where it is required to find the parameters of the incident (converging) and scattered (diverging) spherical waves, at which the total energy flux is zero. However, this approach is difficult to generalize in the case of 3D nanoparticles of a more complex shape, since, in this case, the field of the perfect nonradiating mode cannot be represented as a superposition of a priori known converging and diverging waves.

Another approach for finding perfect nonradiating modes can be the analysis of the spatial structure of two arbitrary solutions of sourceless Maxwell equations, $\mathbf{E}_1$, $\mathbf{H}_1$, and $\mathbf{E}_2$, $\mathbf{H}_2$ in free unbounded spaces with permittivities ε_1, ε_2 in order to find a surface S where the tangential components of the fields are equal, $(E_{1,tan} - E_{2,tan})|_S = 0$, $(H_{1,tan} - H_{2,tan})|_S = 0$. If such a surface can be found, then it can be considered as the surface of a dielectric particle.

As a result, if the interior of such a surface is replaced by a substance with a permittivity of ε_1, then the field $\mathbf{E}_2$ outside this surface will not change, that is, the particle will be invisible (see Figure 2).

As can be seen from the above, perfect nonradiating modes possess fully different physics than quasinormal modes and have no analogs. In particular, they differ from the so-called anapole states [17,20–25] in that their field outside the particle is different from zero and has a well-defined expansion over spherical (5) or spheroidal (15) harmonics. These modes also differ from high-Q supercavity modes or quasi-BIC states because perfect modes do not radiate at all. The perfect modes are closest to strange Neumann–Wigner modes [29], but unlike the latter, the optical potential of a nanoparticle, $V = k_0^2(1 - \varepsilon(\mathbf{r}))$, differs from the vacuum value only in a bounded region of space, fundamentally distinguishing perfect nonradiating modes from Neumann–Wigner modes [29]. In addition, perfect nonradiating modes are vector ones in contrast to the scalar wave functions in quantum mechanics.

Due to the extremely small scattered power and unlimited radiation Q factors, our finding paves the way for the development of new nano-optical devices, with a high concentration of field inside nanoparticles and extremely small radiative losses, including low threshold nanolasers, biosensors, parametric amplifiers, and nanophotonics quantum circuits.

Institutional Review Board Statement: Not applicable.

Data Availability Statement: Not applicable.

Conflicts of Interest: The authors declare no conflict of interest.

Appendix A

Theory of Perfect Nonradiating Modes in Dielectric Sphere

In the axisymmetric nonmagnetic case $m = 0$, there is no dependence on φ, and only the azimuthal component of the magnetic field H_φ is nonzero, so inside the sphere one can write [39]

$$
\begin{aligned}
H_\varphi^{in} &= A \frac{k_1}{i\omega} \frac{\partial P_n(\cos\theta)}{\partial\theta} j_n(k_1 r) \\
E_r^{in} &= -An(n+1)P_n(\cos\theta)\frac{j_n(k_1 r)}{k_1 r} \\
E_\theta^{in} &= -A\frac{\partial P_n(\cos\theta)}{\partial\theta}\frac{[k_1 r j_n(k_1 r)]'}{k_1 r}
\end{aligned}
\tag{A1}
$$

Here, for the spherical harmonics with $m = 0$, we have used their expression in terms of the Legendre polynomials, $Y_{n0}(\theta,\varphi) = P_n(\cos\theta)$, $k_1 = \sqrt{\varepsilon}k_0$, where k_0 is the wave number in the vacuum, j_n are the spherical Bessel functions, and A is the amplitude of the perfect nonradiating mode inside the sphere. Time dependence, $\sim e^{-i\omega t}$, is assumed everywhere.

Outside the sphere (in a vacuum, $\varepsilon = 1$), we are looking for a solution in exactly the same nonsingular form (and this is a novelty!) with the replacement $k_1 \rightarrow k_0$:

$$
\begin{aligned}
H_\varphi^{out} &= B \frac{k_0}{i\omega} \frac{\partial P_n(\cos\theta)}{\partial\theta} j_n(k_0 r) \\
E_r^{out} &= -Bn(n+1)P_n(\cos\theta)\frac{j_n(k_0 r)}{k_0 r} \\
E_\theta^{out} &= -B\frac{\partial P_n(\cos\theta)}{\partial\theta}\frac{[k_0 r j_n(k_0 r)]'}{k_0 r}
\end{aligned}
\tag{A2}
$$

In (A2), B is the amplitude of a perfect nonradiative mode outside the sphere.

On the boundary of the sphere $r = R$, the tangential components of the fields must be continuous, that is, for any $0 < \theta < \pi$, the following conditions must be met:

$$
\begin{aligned}
A \frac{k_1}{i\omega} \frac{\partial P_n(\cos\theta)}{\partial\theta} j_n(k_1 R) &= B \frac{k_0}{i\omega} \frac{\partial P_n(\cos\theta)}{\partial\theta} j_n(k_0 R) \\
A \frac{\partial P_n(\cos\theta)}{\partial\theta} \frac{1}{k_1 R}[k_1 R j_n(k_1 R)]' &= B \frac{\partial P_n(\cos\theta)}{\partial\theta} \frac{1}{k_0 R}[k_0 R j_n(k_0 R)]'
\end{aligned}
\tag{A3}
$$

Using the orthogonality of the Legendre polynomials, the system of equations that determine the eigenfrequencies of perfect nonradiating modes can be written as:

$$Ak_1 j_n(k_1 R) = Bk_0 j_n(k_0 R); A\frac{1}{k_1 R}[k_1 R j_n(k_1 R)]' = B\frac{1}{k_0 R}[k_0 R j_n(k_0 R)]' \qquad (A4)$$

The nontrivial solutions of (A4), i.e., the perfect nonradiating modes, exist if the determinant of (A4) is equal to zero:

$$\varepsilon j_n\left(\sqrt{\varepsilon}X\right)[X\, j_n(X)]' - j_n(X)[Z\, j_n(Z)]'\Big|_{Z=\sqrt{\varepsilon}X} = 0 \qquad (A5)$$

where $X = k_0 R$ is a size parameter.

For each $\varepsilon > 1$ and $n > 1$, Equation (A5) has an infinite number of real roots, indicating the existence of perfect nonradiating modes, and where the field distributions take the form:

$$\begin{aligned} H_\varphi^{in} &= P_n^1(\cos\theta) j_n(k_1 r), \text{ inside sphere, } r < R \\ H_\varphi^{out} &= P_n^1(\cos\theta)\frac{j_n(k_1 R)}{j_n(k_0 R)} j_n(k_0 r), \text{ outside sphere, } r > R \end{aligned} \qquad (A6)$$

As an example, Figure A1 shows the dependencies of the left side of (A5) on the size parameter X for a sphere with permittivity $\varepsilon = 10$.
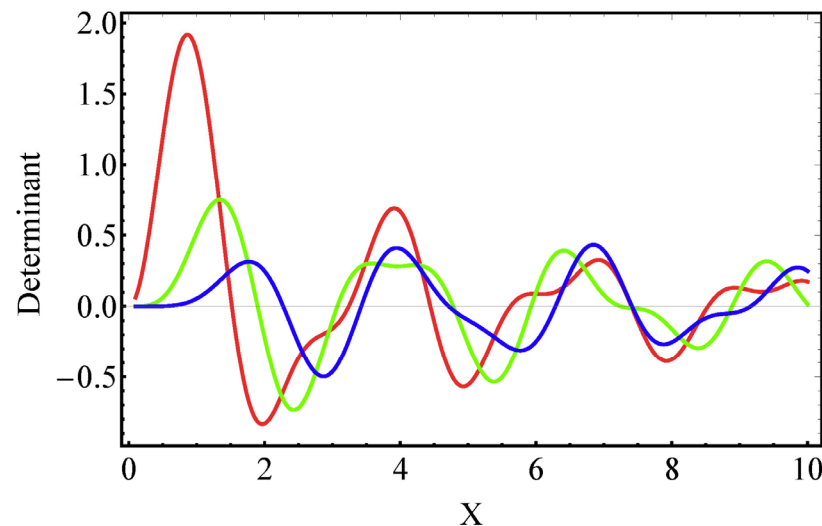

Figure A1. Dependences of the left side of (A5) on the size parameter $X = k_0 R$ for a sphere with permittivity $\varepsilon = 10$ for $n = 1$ (red), $n = 2$ (green), and $n = 3$ (blue).

Figure A1 shows an infinite set of real roots that correspond to the perfect nonradiating modes.

The dependence of the radial part of usual and perfect non-radiating modes on the radius is shown in Figure 1 of the article. Figure A2 shows the spatial distribution of Re$H\varphi$ in the perfect nonradiating mode and the usual mode in a sphere with $\varepsilon = 10$.

It is clearly seen from Figure A2 that the perfect mode exists, has a sensible spatial distribution, and decreases at infinity, while the usual quasinormal mode increases exponentially at infinity.

Thus, the existence of the perfect nonradiating modes in the dielectric sphere has been rigorously proved.
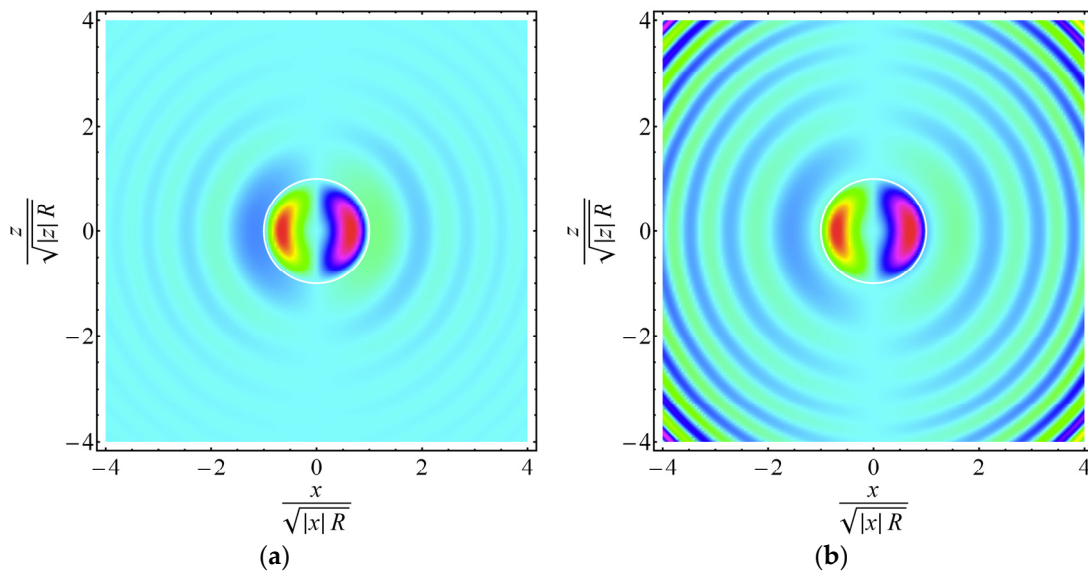
Figure A2. Spatial distribution of ReH_φ in (**a**) the perfect nonradiating PTM$_{101}$ mode (k_0R = 1.51893) and (**b**) the usual TM$_{101}$ mode (k_0R = 1.35715−0.160978 i) in a sphere of the radius R with ε = 10.

Appendix B

Appendix B.1. Theory of Perfect Nonradiating Modes in Dielectric Spheroids

Apparently, perfect nonradiating modes exist for axisymmetric bodies of an arbitrary shape. It is precisely shown below that such modes exist for arbitrary spheroids with semiaxes *a* and *b*, having a volume equal to the volume of a sphere of the radius R and a surface described by the equation:

$$(\rho/b)^2 + (z/a)^2 = 1; a = Rt^{2/3}; b = Rt^{-1/3} \tag{A7}$$

where *t* = *a/b*. For *t* < 1, we have an oblate spheroid, and for *t* > 1, it is an elongated one.

The eigenvalues and eigenfunctions of the perfect nonradiating modes of such spheroids can be found by solving sourceless Maxwell equations in the prolate spheroidal coordinates ξ, η, φ [34,35]. In these coordinates, the surface of the spheroid (A7) is determined by the condition:

$$\xi = \xi_0 = a/\sqrt{a^2 - b^2} \tag{A8}$$

In spheroidal coordinates, the variables can be separated, and solutions of Maxwell's equations can be represented as an expansion over spheroidal wave functions.

Appendix B.2. TM Polarization, Non-Magnetic Case

In the case of TM polarization, for a single nonzero component of the magnetic field, one can write

$$H_{1,\varphi} = \sum_{n=1}^{\infty} a_n PS_{n1}(c_1, \eta) S_{n1}(c_1, \xi), c_1 = k_0 R\sqrt{\varepsilon}\sqrt{t^2 - 1}/t^{1/3} \text{ inside nanoparticle}, 1 < \xi < \xi_0$$
$$H_{2,\varphi} = \sum_{n=1}^{\infty} b_n PS_{n1}(c_0, \eta) S_{n1}(c_0, \xi), c_0 = k_0 R\sqrt{t^2 - 1}/t^{1/3} \text{ everywhere}, \xi > 1 \tag{A9}$$

where $PS_{n1}(c, \eta)$ are the angular spheroidal functions and $S_{n1}(c, \xi)$ are the radial spheroidal functions of the first kind [34].

The tangential component of the electric field looks like:

$$E_{1,\eta} = \frac{1}{\varepsilon} \frac{2i}{k_0 d(\xi^2 - \eta^2)^{1/2}} \sum_{n=1}^{\infty} a_n PS_{n1}(c_1, \eta) \frac{\partial (\xi^2 - 1)^{1/2} S_{n1}(c_1, \xi)}{\partial \xi} \tag{A10}$$

inside nanoparticles, $\xi < \xi_0$, and

$$E_{2,\eta} \;=\; \frac{2i}{k_0 d(\xi^2 - \eta^2)^{1/2}} \sum_{n=1}^{\infty} b_n PS_{n1}(c_0, \eta) \frac{\partial \left(\xi^2 - 1\right)^{1/2} S_{n1}(c_0, \xi)}{\partial \xi} \tag{A11}$$

everywhere, $\xi > 1$. In (A10) and (A11) and elsewhere, $d \;=\; 2\sqrt{a^2 - b^2}$.

After multiplication by angular harmonics, integration over η, and application of the orthogonality condition for angular spheroidal functions,

$$\int_{-1}^{1} d\eta \, PS_{n1}(c_1, \eta) PS_{m1}(c_1, \eta) \;=\; \delta_{nm} NN_n \;=\; \delta_{nm} \frac{2n(n+1)}{2n+1} \tag{A12}$$

the conditions for the continuity of the magnetic and electric fields at the spheroid boundary $\xi = \xi_0$ take the form:

$$a_n NN_n S_{n1}(c_1, \xi_0) \;=\; \sum_{p=1}^{\infty} \Pi_{np}(c_1, c_0) S_{p1}(c_0, \xi_0) b_p \tag{A13}$$

$$\frac{1}{\varepsilon} a_n NN_n SD_n(c_1, \xi_0) \;=\; \sum_{p=1}^{\infty} \Pi_{np}(c_1, c_0) SD_p(c_0, \xi_0) b_p;$$

$$\Pi_{n,p}(c_1, c_0) \;=\; \int_{-1}^{1} d\eta \, PS_{n1}(c_1, \eta) PS_{p1}(c_0, \eta) \tag{A14}$$

$$SD_n(c, \xi_0) \;=\; \partial_{\xi_0}\!\left(\left(\xi_0^2 - 1\right)^{1/2} S_{p1}(c, \xi_0) \right)$$

Figure A3 shows the dependence of the overlap integral $\prod_{n,p}(c_1, c_0)$ of angular spheroidal functions on the indices n, p.

Figure A3 shows that:

1. Only modes with the same parity interact with each other;
2. For each mode, interaction is essential only with the nearest modes of the same parity, $2k \Leftrightarrow 2(k \pm 1)$; $2k + 1 \Leftrightarrow 2(k \pm 1) + 1$.

This circumstance simplifies calculations since matrices of finite dimension 3×3 can be used to calculate eigenfrequencies with high accuracy.

Eliminating a_n from (A13) and (A14), we obtain a homogeneous system of equations for the coefficients b_p, determining the magnetic field outside the particle:

$$\sum_{p=1}^{\infty} \Pi_{np}(c_1, c_0) \left(\varepsilon SD_{p1}(c_0, \xi_0) S_{n1}(c_1, \xi_0) - S_{p1}(c_0, \xi_0) SD_{n1}(c_1, \xi_0) \right) b_p \;=\; 0 \tag{A15}$$

The compatibility condition of (A15) allows one to find the modes and eigenfrequencies of the perfect nonradiating modes shown in Figures 6 and 7 of the article.
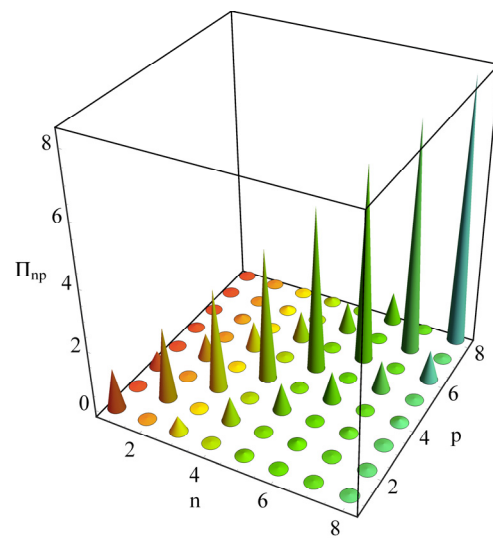
Figure A3. Dependence of the overlap integral of angular spheroidal functions in an elongated spheroid $\prod_{n,p}(c_1,c_0)$ on indices. $c_1 = 4$, $c_0 = c_1/\sqrt{\varepsilon} = 0.5657$, $\varepsilon = 50$.

Appendix B.3. TE Polarization, Non-Magnetic Case

In this case, the only nonzero component of the electric field can be written in the form:

$$
\begin{aligned}
E_{1,\varphi} &= \sum_{n=1}^{\infty} a_n PS_{n1}(c_1,\eta)S_{n1}(c_1,\xi), c_1 = k_0 R\sqrt{\varepsilon}\sqrt{t^2-1}/t^{1/3} \text{ inside nanoparticle, } 1 < \xi < \xi_0 \\
E_{2,\varphi} &= \sum_{n=1}^{\infty} b_n PS_{n1}(c_0,\eta)S_{n1}(c_0,\xi), c_0 = k_0 R\sqrt{t^2-1}/t^{1/3} \text{ everywhere, } \xi > 1
\end{aligned}
\tag{A16}
$$

Repeating the reasoning for TM polarization (see Appendix B.2) for the coefficients b_p, determining the electric field outside the particle, we obtain a homogeneous system of equations:

$$
\sum_{p=1}^{\infty} \Pi_{np}(c_1,c_0)\big(SD_{p1}(c_0,\xi_0)S_{n1}(c_1,\xi) - S_{p1}(c_0,\xi_0)SD_{n1}(c_1,\xi_0)\big)b_p = 0
\tag{A17}
$$

that differs from the dispersion Equation (A15) only by the absence of ε in the parenthesis.

References

1. Novotny, L.; Van Hulst, N. Antennas for light. *Nat. Photon.* **2011**, *5*, 83–90. [CrossRef]
2. Biagioni, P.; Huang, J.S.; Hecht, B. Nanoantennas for visible and infrared radiation. *Rep. Prog. Phys.* **2012**, *75*, 024402. [CrossRef] [PubMed]
3. Tiguntseva, E.; Koshelev, K.; Furasova, A.; Tonkaev, P.; Mikhailovskii, V.; Ushakova, E.V.; Baranov, D.G.; Shegai, T.; Zakhidov, A.A.; Kivshar, Y.; et al. Room-Temperature Lasing from Mie-Resonant Nonplasmonic Nanoparticles. *ACS Nano* **2020**, *14*, 8149. [CrossRef] [PubMed]
4. Mylnikov, V.; Ha, S.T.; Pan, Z.; Valuckas, V.; Paniagua-Dominguez, R.; Demir, H.V.; Kuznetsov, A.I. Lasing Action in Single Subwavelength Particles Supporting Supercavity Modes. *ACS Nano* **2020**, *14*, 7338. [CrossRef] [PubMed]
5. Zheng, K.; Zhang, Z.; Qin, F.; Xu, Y. Invisible Mie scatterer. *Opt. Lett.* **2021**, *46*, 5248–5251. [CrossRef]
6. Liu, Z.; Zhou, Y.; Guo, Z.; Zhao, X.; Luo, M.; Li, Y.; Wu, X. Ultrahigh Q-Guided Resonance Sensor Empowered by Near Merging Bound States in the Continuum. *Photonics* **2022**, *9*, 852. [CrossRef]
7. Barreda, A.I.; Sanz, J.M.; Gonzalez, F. Using linear polarization for sensing and sizing dielectric nanoparticles. *Opt. Express* **2015**, *23*, 9157. [CrossRef]
8. García-Cámara, B.; Gómez-Medina, R.; Sáenz, J.J.; Sepúlveda, B. Sensing with magnetic dipolar resonances in semiconductor nanospheres. *Opt. Express* **2013**, *23*, 23007. [CrossRef]
9. Barreda, A.; Vitale, F.; Minovich, A.; Ronning, C.; Staude, I. Applications of Hybrid Metal-Dielectric Nanostructures: State of the Art. *Adv. Photonics Res.* **2022**, *3*, 2100286. [CrossRef]
10. Grinblat, G.; Li, Y.; Nielsen, M.P.; Oulton, R.F.; Maier, S.A. Efficient third harmonic generation and nonlinear subwavelength imaging at a higher-order anapole mode in a single germanium nanodisk. *ACS Nano* **2017**, *11*, 953–960. [CrossRef]

11. Hsu, C.W.; Zhen, B.; Lee, J.; Chua, S.-L.; Johnson, S.G.; Joannopoulos, J.D.; Soljačic, M. Observation of trapped light within the radiation continuum. *Nature* **2013**, *499*, 188. [CrossRef] [PubMed]

12. Hsu, C.; Zhen, B.; Stone, A.; Joannopoulos, J.D.; Soljačic, M. Bound states in the continuum. *Nat. Rev. Mater.* **2016**, *1*, 16048. [CrossRef]

13. Koshelev, K.; Favraud, G.; Bogdanov, A.; Kivshar, Y.; Fratalocchi, A. Nonradiating photonics with resonant dielectric nanostructures. *Nanophotonics* **2019**, *8*, 725. [CrossRef]

14. Carletti, L.; Koshelev, K.; de Angelis, C.; Kivshar, Y. Giant nonlinear response at the nanoscale driven by bound states in the continuum. *Phys. Rev. Lett.* **2018**, *121*, 33903. [CrossRef]

15. Rybin, M.V.; Koshelev, K.L.; Sadrieva, Z.F.; Samusev, K.B.; Bogdanov, A.A.; Limonov, M.F.; Kivshar, Y.S. High-*Q* supercavity modes in subwavelength dielectric resonators. *Phys. Rev. Lett.* **2017**, *119*, 243901. [CrossRef]

16. Odit, M.; Koshelev, K.; Gladyshev, S.; Ladutenko, K.; Kivshar, Y.; Bogdanov, A. Observation of supercavity modes in subwavelength dielectric resonators. *Adv. Mater.* **2021**, *33*, 2003804. [CrossRef]

17. Zel'dovich, Y.B. Electromagnetic interaction with parity violation. *JETP* **1957**, *6*, 1184.

18. McLean, J.S.; Foltz, H. The Relationship between Cartesian Multipoles and Spherical Wavefunction Expansions with Application to Wireless Power Transfer. In Proceedings of the Antenna Measurement Techniques Association Symposium (AMTA), Newport, RI, USA, 2–5 November 2020; pp. 1–6.

19. Radescu, E., Jr.; Vaman, G. Cartesian Multipole Expansions and Tensorial Identities. *Prog. Electromagn. Res. B* **2012**, *36*, 89. [CrossRef]

20. Yang, Y.; Bozhevolnyi, S.I. Nonradiating anapole states in nanophotonics: From fundamentals to applications. *Nanotechnology* **2019**, *30*, 204001. [CrossRef]

21. Manna, U.; Sugimoto, H.; Eggena, D.; Coe, B.; Wang, R.; Biswas, M.; Fujii, M. Selective excitation and enhancement of multipolar resonances in dielectric nanospheres using cylindrical vector beams. *J. Appl. Phys.* **2020**, *127*, 033101. [CrossRef]

22. Parker, J.A.; Sugimoto, H.; Coe, B.; Eggena, D.; Fujii, M.; Scherer, N.F.; Gray, S.K.; Manna, U. Excitation of Nonradiating Anapoles in Dielectric Nanospheres. *Phys. Rev. Lett.* **2020**, *124*, 097402. [CrossRef] [PubMed]

23. Luk'yanchuk, B.; Paniagua-Domínguez, R.; Kuznetsov, A.I.; Miroshnichenko, A.E.; Kivshar, Y.S. Hybrid anapole modes of high-index dielectric nanoparticles. *Phys. Rev. A.* **2017**, *95*, 063820. [CrossRef]

24. Wei, L.; Xi, Z.; Bhattacharya, N.; Urbach, H.P. Excitation of the radiationless anapole mode. *Optica* **2016**, *3*, 799. [CrossRef]

25. Lu, Y.; Xu, Y.; Ouyang, X.; Xian, M.; Cao, Y.; Chen, K.; Li, X. Cylindrical vector beams reveal radiationless anapole condition in a resonant state. *Opto-Electron. Adv.* **2021**, *5*, 210076. [CrossRef]

26. Diaz-Escobar, E.; Bauer, T.; Pinilla-Cienfuegos, E.; Barreda, Á.I.; Griol, A.; Kuipers, L.; Martínez, A. Radiationless anapole states in on-chip photonics. *Light Sci. Appl.* **2021**, *10*, 204. [CrossRef]

27. Klimov, V. Manifestation of extremely high-*Q* pseudo-modes in scattering of a Bessel light beam by a sphere. *Opt. Lett.* **2020**, *45*, 4300. [CrossRef]

28. Bohren, C.; Huffmann, D. *Absorption and Scattering of Light by Small Particles*; John Wiley: New York, NY, USA, 1983.

29. von Neumann, J.; Wigner, E.P. Uber merkwiirdige diskrete Eigenwerte. *Phys. Z.* **1929**, *30*, 465.

30. Arai, M.; Uchiyama, J. On the von Neumann and Wigner Potentials. *J. Differ. Equ.* **1999**, *157*, 348. [CrossRef]

31. Schinke, C.; Peest, P.C.; Schmidt, J.; Brendel1, R.; Bothe, K.; Vogt, M.R.; Kröger, I.; Winter, S.; Schirmacher, A.; Lim, S.; et al. Uncertainty analysis for the coefficient of band-to-band absorption of crystalline silicon. *AIP Adv.* **2015**, *5*, 67168. [CrossRef]

32. Weiting, F.; Yixun, Y. Temperature effects on the refractive index of lead telluride and zinc selenide. *Infrared Phys.* **1990**, *30*, 371. [CrossRef]

33. Krishnamoorthy, H.N.S.; Adamo, G.; Yin, J.; Savinov, V.; Zheludev, N.I.; Soci, C. Infrared dielectric metamaterials from high refractive index chalcogenides. *Nat. Comm.* **2020**, *11*, 1692.

34. Meixner, J.; Schäfke, F.W. *Mathieusche Funktionen und Sphäroidfunktionen mit Anwendungen auf Physikalische und Technische Probleme*; Grundlehren der mathematischen Wissenschaften; Springer: Berlin/Heidelberg, Germany, 1954; Volume 71, 432p.

35. Li, L.-W.; Kang, X.-K.; Leong, M.-S. *Spheroidal Wave Functions in Electromagnetic Theory*; John Wiley & Sons, Inc.: Hoboken, NJ, USA, 2002.

36. van Bladel, J. On the resonances of a dielectric resonator of very high permittivity. *IEEE Trans. Microw. Theory Tech.* **1975**, *MTT-23*, 199–208. [CrossRef]

37. Klimov, V.V.; Guzatov, D.V. Perfect Nonradiating Modes in Dielectric Nanofiber with Elliptical Cross-Section. Available online: https://arxiv.org/abs/2204.13327v2 (accessed on 2 May 2022).

38. Guzatov, D.V.; Klimov, V.V. The influence of chiral spherical particles on the radiation of optically active molecules. *New J. Phys.* **2012**, *14*, 123009. [CrossRef]

39. Stratton, J.A. *Electromagnetic Theory*; McGraw-Hill Book Company: New York, NY, USA; London, UK, 1941; 557p.